Monthly Notices
of the
ROYAL ASTRONOMICAL SOCIETY

Mon. Not. R. Astron. Soc. **416,** 2949–2961 (2011) doi:10.1111/j.1365-2966.2011.19243.x

The OGLE view of microlensing towards the Magellanic Clouds – IV. OGLE-III SMC data and final conclusions on MACHOs⋆

L. Wyrzykowski,[1,2]† J. Skowron,[2,3] S. Kozłowski,[2,3] A. Udalski,[2] M. K. Szymański,[2] M. Kubiak,[2] G. Pietrzyński,[2,4] I. Soszyński,[2] O. Szewczyk,[2,4] K. Ulaczyk,[2] R. Poleski[2] and P. Tisserand[5]

[1]*Institute of Astronomy, University of Cambridge, Madingley Road, Cambridge CB3 0HA*
[2]*Warsaw University Astronomical Observatory, Al. Ujazdowskie 4, 00-478 Warszawa, Poland*
[3]*Department of Astronomy, The Ohio State University, 140 West 18th Avenue, Columbus, OH 43210, USA*
[4]*Universidad de Concepción, Departamento de Astronomia, Casilla 160-C, Concepción, Chile*
[5]*Research School of Astronomy and Astrophysics, Australian National University, Cotter Road, Weston Creek, ACT 2611, Australia*

Accepted 2011 June 13. Received 2011 June 13; in original form 2011 March 23

ABSTRACT

In this fourth part of the series presenting the Optical Gravitational Lensing Experiment (OGLE) microlensing studies of the dark matter halo compact objects (MACHOs), we describe results of the OGLE-III monitoring of the Small Magellanic Cloud (SMC). Three sound candidates for microlensing events were found and yielded the optical depth $\tau_{\rm SMC-OIII} = 1.30 \pm 1.01 \times 10^{-7}$, consistent with the expected contribution from Galactic disc and SMC self-lensing. We report that event OGLE-SMC-03 is most likely a thick-disc lens candidate, the first of such type found towards the SMC. In this paper we also combined all OGLE Large Magellanic Cloud and SMC microlensing results in order to refine the conclusions on MACHOs. All but one of the OGLE events are most likely caused by the lensing by known populations of stars; therefore, we concluded that there is no need for introducing any special dark matter compact objects in order to explain the observed event rates. Potential black hole event indicates that similar lenses can contribute only about 2 per cent to the total mass of the halo, which is still in agreement with the expected number of such objects.

Key words: Galaxy: halo – Galaxy: structure – dark matter.

1 INTRODUCTION

Campaigns like Optical Gravitational Lensing Experiment (OGLE), MACHO or Expérience de Recherche d'Objets Sombres (EROS) were all founded nearly 20 years ago primarily to settle the question whether dark matter resided in the galactic halo in the form of compact objects (MACHOs). The background theory of the method employing gravitational microlensing was provided by Bohdan Paczyński (Paczyński 1986), and in subsequent years Paczyński himself advocated and supported the creation of large-scale photometric surveys towards the Magellanic Clouds. The Large and Small Magellanic Clouds (LMC and SMC, respectively) were considered the best targets for such studies, as with a moderate telescope size the stars of the clouds were easily resolved and hence formed a perfect background for the hunt for microlensing events. These are unique and temporal brightening events observed on a source background star caused by the gravitational lensing phenomenon in which the lensing object is located in front of the background star.

In the most generic case of a point lens mass and a point source, the gravitational amplification of the background light is described by the equation (after Paczyński 1996)

$$A = \frac{u^2+2}{u\sqrt{u^2+4}} \qquad \text{and} \qquad u = \sqrt{u_0^2 + \frac{(t-t_0)^2}{t_{\rm E}^2}}, \tag{1}$$

where t_0 is the time of the maximum of the peak, $t_{\rm E}$ is the Einstein radius crossing time (event time-scale) and u_0 is the event impact parameter.

Parameter $t_{\rm E}$ is the only parameter linked with the physical properties of the source–lens system and is dependent on the lens mass, the lens and source distances, and the relative velocity between lens and source. This means that, in principle, a single microlensing event cannot provide any information regarding the lensing object. Additional data are possible only in case of non-standard events like binary lens/source or those showing a parallax effect. Hence, in studying the mass distribution of lenses, microlensing events are

⋆Based on observations obtained with the 1.3-m Warsaw telescope at the Las Campanas Observatory of the Carnegie Institution of Washington.

†E-mail: wyrzykow@ast.cam.ac.uk, name pronunciation: *Woocash Vizhikovsky*

regarded only in groups. The statistical value related to the total mass enclosed in the volume towards the background sources is the microlensing optical depth, τ:

$$\tau = \frac{\pi}{2N_* T_{\rm obs}} \sum_{i}^{N_{\rm ev}} \frac{t_{{\rm E}i}}{\epsilon(t_{{\rm E}i})}, \quad (2)$$

where $T_{\rm obs}$ is the time-span of all observations, N_* is the total number of monitored stars, $N_{\rm ev}$ is the total number of events, each with time-scale $t_{{\rm E}i}$ and detection efficiency $\epsilon(t_{{\rm E}i})$.

In the case of the Magellanic Clouds, the overall optical depth can be composed with contributions from lenses at various levels. Apart from the hypothetical dark matter compact objects, there can also be a contribution to the optical depth from luminous lenses from the disc of our Galaxy and from the frontal side of the cloud itself [i.e. self-lensing (SL)].

Observations and studies of the pixel-lensing microlensing events towards M31 are still not conclusive with respect to the amount of SL and MACHO lenses (see Calchi Novati 2010b, for recent review). However, the most recent analysis of the data tends to be inclined towards SL as being the only explanation of the observed signal (Calchi Novati 2010a).

The most recent studies of the data gathered by microlensing surveys towards the LMC suggest that the contribution from dark matter compact objects with masses below 10 $M_\odot$ can be practically ruled out. The upper limit on MACHO abundance in the halo was set to 6–7 per cent by the EROS (Tisserand et al. 2007) and OGLE groups (Wyrzykowski et al. 2011) (see Moniez 2010, for review). The core of the detected microlensing signal seems to come from the SL events, as suggested already in Sahu (1994b, a).

The LMC SL effect is relatively well understood thanks to the convenient, almost face-on alignment of the LMC towards us. The studies by Mancini et al. (2004), Calchi Novati et al. (2009) and Calchi Novati & Mancini (2011) showed that the average SL optical depth is of the order of 0.4×10^{-7}, which is consistent with what was measured in OGLE-II (Wyrzykowski et al. 2009, hereafter Paper I) and OGLE-III data (Wyrzykowski et al. 2011, hereafter Paper III).

The situation with the SMC is more complicated. This dwarf galaxy seems to be elongated and is stretched out along the line of sight, which produces a much higher SL optical depth. Some estimates by Palanque-Delabrouille et al. (1998) and Graff & Gardiner (1999) place this value at at least 1.0×10^{-7}, but it can actually be much higher. Microlensing studies of the SMC tend to confirm this with their typically higher event rates (Tisserand et al. 2007; Wyrzykowski et al. 2010, hereafter Paper II), compared with those of the LMC.

In this paper, we conclude the series of studies of the OGLE microlensing data towards both the Magellanic Clouds with the analysis of the 8 years of observations of the SMC in the course of the OGLE-III project. We attempt to finalize the investigation of the subtle topic of dark matter compact halo objects, providing the result from the currently best and most suitable data set.

The paper is organized as follows. First, the OGLE-III data used for the analysis are presented. Then, we describe the method applied for finding the microlensing events and its results with a detailed description and study of each event found. This is followed by a calculation of the optical depth and a discussion of the results.

2 OBSERVATIONAL DATA

The photometric data used in this study were collected during the third phase of the OGLE project (2001–09) with the 1.3-m Warsaw telescope located at Las Campanas Observatory, Chile, operated by the Carnegie Institution of Washington. The 'second generation' camera comprised of eight SITe2048 × 4096 CCD detectors with 15-μm pixels, resulting in 0.26 arcsec pixel^{-1} and 35 × 35 arcmin total field of view. The details on the instrumentation set-up can be found in Udalski (2003).

The central regions and the outskirts of the SMC were covered by 41 fields, giving a total of 14 deg^2. The map of the fields is shown in Fig. 1. The statistical details of the fields are gathered in Table 1 with the following information: the coordinates of their centres, the number of 'good' template objects in the *I* band, the blending-corrected number of stars (see Section 5) and the mean number of all objects visible on a single CCD (of eight) used for assigning the blending density level. 'Good' objects are the template objects with at least 80 good data points (excluding measurements with very large error bars) and mean magnitude brighter than 21.0 mag (chosen as a mean peak of the observed luminosity functions).

The very first observations of the SMC within the OGLE-III phase were taken in 2001 June (JD = 245 2085), except field SMC140 (started in July 2004), and continued until 2009 May (JD = 245 4954). Most of the observations were taken through the Cousins *I*-band filter with exposure time of 180 s and a mean seeing of 1.36 arcsec. Between 583 and 762 measurements were gathered in each field with an average sampling varying from 2.0 to 3.0 d between subsequent frames (excluding the gaps between the seasons). The only exception is field SMC128 which was observed 1228 times with an average sampling of 1.6 d. Additionally, between 47 and 114 observations per field were obtained in Johnson *V* band with integration time of 225 s and a mean seeing of 1.39 arcsec. First *V*-band observations were taken in 2004 November (JD = 245 3314), and since then *V* filter frames were taken regularly. The average sampling frequency in the *V* band was between 4.6 and 10.3 d.

The image reduction pipeline used an image subtraction technique and was based on difference image analysis (DIA; Alard & Lupton 1998; Woźniak 2000). The data used in this work come from the final reductions calibrated to the standard system. The template images used for subtraction were composed from selected best individual frames resulting in a seeing of around 0.9 and 1.0 arcsec for *I* and *V* bands, respectively. The full description of the reduction techniques, photometric calibration and astrometric transformations can be found in Udalski et al. (2008).

Photometric errors produced by the difference imaging process were adjusted as described in Paper I by deriving a magnitude-dependent correction factor (CF) using the constant stars. For each SMC field and each filter ($f = I, V$), we found parameters γ_f and ϵ_f, which correct the original error bar according to the formula

$$\sigma_{{\rm mag}_f {\rm cor}} = \sqrt{(\gamma_f \sigma_{{\rm mag}_f})^2 + \epsilon_f^2}, \quad (3)$$

where $\sigma_{\rm mag}$ is the original error bar returned by DIA.

Error-correction parameters averaged over all SMC fields yielded $\langle\gamma_I\rangle = 1.040\,31$, $\langle\epsilon_I\rangle = 0.004\,148\,52$, $\langle\gamma_V\rangle = 0.867\,849$ and $\langle\epsilon_V\rangle = 0.002\,6929$. Table 2 shows the error-correction coefficients for the first few fields. The full table can be found on the OGLE website.[1]

[1] http://ogle.astrouw.edu.pl/

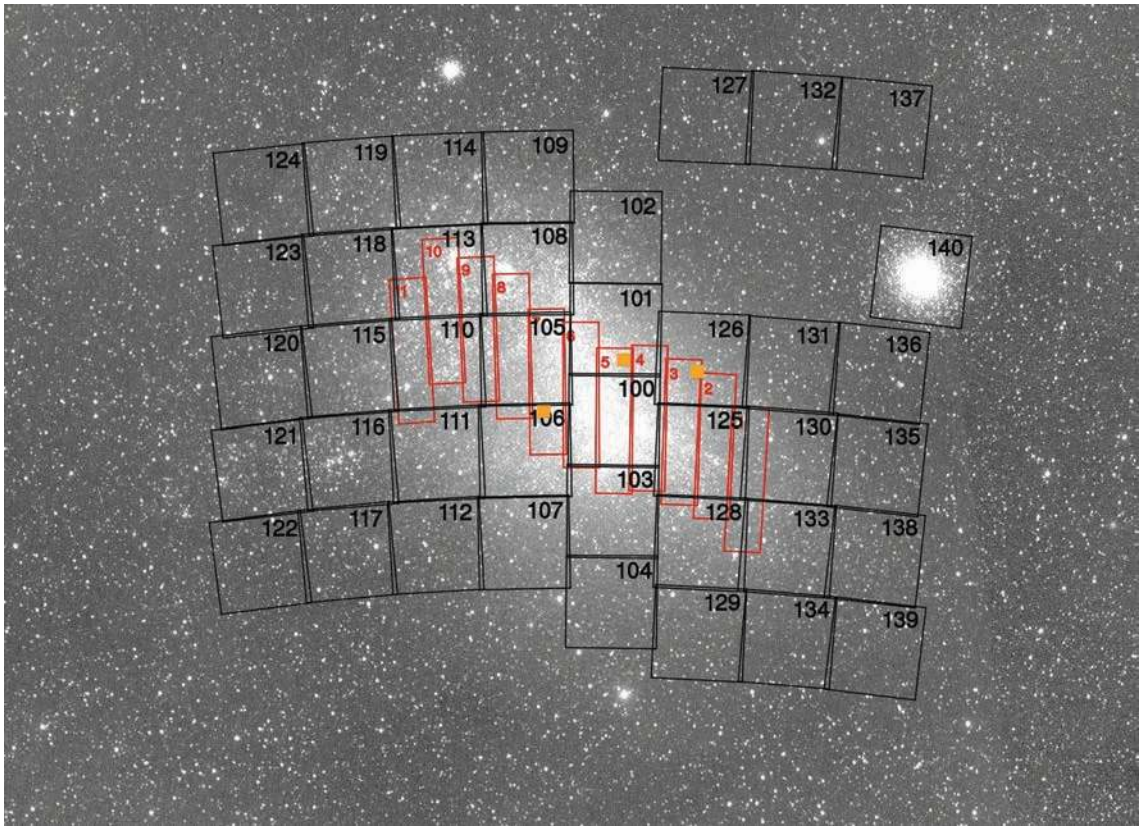

Figure 1. Positions of the OGLE-III SMC fields (black). Also shown are all OGLE-II fields (red rectangles). The three small filled squares show the positions of the *HST* fields used for our blending determination. Background image credit: ASAS all sky survey.

Table 1. OGLE-III SMC fields.

Field	α_{J2000}	δ_{J2000}	$N_{*good}(10^3)$ Tpl	Real	$\langle \log N_{all_{CCD}} \rangle$	Field	α_{J2000}	δ_{J2000}	$N_{*good}(10^3)$ Tpl	Real	$\langle \log N_{all_{CCD}} \rangle$
SMC100	0:50:02.9	−73:08:40	469.8	550.5	4.81	SMC121	1:22:01.2	−73:20:35	28.7	29.2	3.60
SMC101	0:50:00.4	−72:33:18	315.5	353.6	4.63	SMC122	1:23:12.8	−73:56:05	19.3	19.6	3.43
SMC102	0:50:05.0	−71:57:26	106.4	111.3	4.18	SMC123	1:20:02.3	−72:09:34	31.3	31.9	3.64
SMC103	0:50:04.8	−73:44:00	249.9	274.8	4.54	SMC124	1:19:09.6	−71:33:44	41.0	41.9	3.74
SMC104	0:50:05.0	−74:19:23	89.9	94.0	4.21	SMC125	0:42:04.2	−73:19:45	309.8	351.3	4.68
SMC105	0:57:49.6	−72:44:41	338.0	378.3	4.66	SMC126	0:42:21.8	−72:44:08	189.2	203.2	4.41
SMC106	0:58:05.5	−73:20:17	314.6	352.7	4.66	SMC127	0:42:54.6	−71:09:03	19.2	19.5	3.43
SMC107	0:58:21.9	−73:55:54	125.0	131.3	4.25	SMC128	0:41:46.2	−73:55:25	172.0	183.4	4.38
SMC108	0:57:32.5	−72:09:24	379.9	434.5	4.71	SMC129	0:41:31.9	−74:30:42	50.4	51.7	3.85
SMC109	0:57:20.9	−71:33:48	111.1	116.6	4.22	SMC130	0:34:06.1	−73:19:39	114.0	119.0	4.20
SMC110	1:05:35.8	−72:44:45	198.1	213.0	4.47	SMC131	0:34:34.0	−72:44:11	65.9	68.0	3.95
SMC111	1:06:06.0	−73:20:14	161.8	171.9	4.36	SMC132	0:35:49.7	−71:08:46	16.7	17.0	3.37
SMC112	1:06:40.9	−73:55:48	92.3	96.1	4.15	SMC133	0:33:36.9	−73:55:24	94.2	97.8	4.10
SMC113	1:05:03.2	−72:09:28	241.6	264.7	4.55	SMC134	0:32:52.5	−74:30:42	39.4	40.2	3.73
SMC114	1:04:36.8	−71:33:42	145.4	153.5	4.29	SMC135	0:26:03.8	−73:19:45	46.4	47.6	3.83
SMC115	1:13:19.4	−72:44:42	87.9	91.4	4.14	SMC136	0:26:48.7	−72:44:14	36.3	37.1	3.71
SMC116	1:14:05.2	−73:20:08	107.4	112.0	4.17	SMC137	0:28:42.4	−71:08:44	14.1	14.3	3.30
SMC117	1:15:00.4	−73:55:44	37.2	38.1	3.77	SMC138	0:25:21.4	−73:55:17	53.8	55.4	3.99
SMC118	1:12:35.3	−72:09:12	72.6	75.2	4.06	SMC139	0:24:16.5	−74:30:48	30.5	31.1	3.63
SMC119	1:11:54.1	−71:33:40	96.6	100.1	4.11	SMC140	0:24:05.1	−72:05:00	301.6	341.8	4.63
SMC120	1:21:05.2	−72:44:46	55.5	56.9	3.87						
								Total	5470 352	5971 776	

Note. Coordinates point to the centre of the field (centre of the mosaic), each being 35×35 arcmin^2. The number of 'good' objects in the template is provided ($N > 80$ and $\langle I \rangle < 21.0$ mag) together with the estimated number of real monitored stars (see Section 5). The mean number of all objects detected on a single CCD used for calculating the density of a field is given in the last column.

Table 2. Error-correction coefficients for each CCD chip of the first four OGLE-III LMC fields for *I* and *V* bands. The full table is available online from the OGLE website.

Field	γ_I	ϵ_I	γ_V	ϵ_V
SMC100.1	0.892	0.0040	0.787	0.0029
SMC100.2	0.903	0.0044	0.764	0.0026
SMC100.3	0.891	0.0042	0.736	0.0027
SMC100.4	0.930	0.0037	0.793	0.0026
SMC100.5	0.911	0.0048	0.758	0.0028
SMC100.6	0.922	0.0043	0.780	0.0026
SMC100.7	0.921	0.0044	0.787	0.0028
SMC100.8	1.026	0.0044	0.840	0.0032
SMC101.1	0.947	0.0040	0.963	0.0029
SMC101.2	0.939	0.0044	0.895	0.0026
SMC101.3	0.951	0.0042	0.916	0.0027
SMC101.4	1.000	0.0037	1.138	0.0026
SMC101.5	1.010	0.0048	1.057	0.0028
SMC101.6	1.043	0.0043	1.100	0.0026
SMC101.7	1.002	0.0044	1.050	0.0028
SMC101.8	1.145	0.0044	1.089	0.0032
SMC102.1	0.944	0.0040	0.827	0.0029
SMC102.2	0.951	0.0044	0.816	0.0026
SMC102.3	0.972	0.0042	0.830	0.0027
SMC102.4	0.977	0.0037	0.901	0.0026
SMC102.5	0.951	0.0048	0.839	0.0028
SMC102.6	1.030	0.0043	0.901	0.0026
SMC102.7	1.005	0.0044	0.908	0.0028
SMC102.8	1.109	0.0044	0.869	0.0032
SMC103.1	0.995	0.0040	0.925	0.0029
SMC103.2	1.002	0.0044	1.015	0.0026
SMC103.3	0.996	0.0042	0.973	0.0027
SMC103.4	1.029	0.0037	0.955	0.0026
SMC103.5	1.019	0.0048	0.885	0.0028
SMC103.6	1.024	0.0043	0.977	0.0026
SMC103.7	1.042	0.0044	1.015	0.0028
SMC103.8	1.121	0.0044	0.962	0.0032
...				

3 SEARCH PROCEDURE

For the SMC OGLE-III data, we applied the same automated pipeline for detecting microlensing events as designed and used in searching through the LMC OGLE-II (Paper I), SMC OGLE-II (Paper II) and LMC OGLE-III (Paper III) data. The procedure for the SMC contains 10 cuts applied to the pre-selected 'good' data (with enough good observations) and limited to the right magnitude level. Table 3 describes all cuts applied to the data for two star samples (defined at cut 0): All Stars – limited to 21 mag (maximum of the observed luminosity functions, i.e. the end of OGLE completeness in these fields) and Bright Stars – limited to 19.3 mag (1 mag below mean red clump position).

In the first cut, for each star sample, we selected light curves with a significant bump over baseline, following the concept of Sumi et al. (2006). Then, we removed all candidates with their baseline colour and magnitude located in the 'blue bumper' region to exclude these most common contaminants related with the Be stars. In cut 3, we chose those light curves for which the standard microlensing fit (with blending parameter fixed, hence index $\mu 4$ in Table 3) was better than a constant line fit. In the following cut, we required that there were at least six data points in the microlensing peak between $t_0 - t_E$ and $t_0 + t_E$.

In cut 5, we fitted the candidate bump also with the simple supernova model (exponential decline) and selected only those for which the χ^2 of the microlensing fit was better (either with blending or without). The number of expected supernovae in the entire OGLE-III coverage of the SMC is around 22 (after Dilday et al. 2010, assuming 20 per cent detection efficiency), and indeed many of the objects removed at this stage resembled supernovae outbursts, some clearly with the host galaxy visible on the OGLE image. In this way, we also removed all other asymmetric bumps. The objects remaining after this step were visually inspected and most of them turned out to be either nova-like events or red-baseline bumpers.

We then checked if the peak of the candidate bump was located within the data span (cut 6). In the next two cuts (7 and 8), we required that the blended microlensing model fit converged and yielded reasonable values, allowing for some negative blending (effect of instrumental origin; see e.g. Smith et al. 2007), and that the $\chi^2/N_{\rm dof}$ of the blended fit was better than 2.6 and for the non-blended fit around the peak better than 4.5.

Finally, we restricted our search of microlensing events to the ones with time-scales between 1 and 1000 d and with impact parameters below 1.

4 RESULTS

Running our search pipeline on the SMC OGLE-III data we found three candidates for microlensing events in All Stars Sample. Two of them were found in the Bright Stars Sample. The three events were dubbed OGLE-SMC-02, OGLE-SMC-03 and OGLE-SMC-04, with the numbers following the numbering started with the single candidate detected in the OGLE-II SMC data (Paper II).

The basic information about these candidates is shown in Table 4. The first two events were detected while ongoing by the Early Warning System (EWS) of OGLE, while the third one was not known before and occurred at the beginning of the OGLE-III when EWS was not yet operating.

Fig. 2 shows the colour–magnitude diagram (CMD) with candidate events found in OGLE-II, OGLE-III and MACHO data. Fig. 3 presents a density of red clump stars of the SMC with marked positions of all candidate events. The light curves of the three OGLE-III events with microlensing model fits are shown in Fig. 4, whereas their finding charts are presented in Fig. 5.

Below we discuss each candidate in detail.

4.1 OGLE-SMC-02

This event was already known before this work as it was detected in real time with the OGLE's EWS and was designated 2005-SMC-001.[2] It was probably one of the longest, brightest and best observed events found to date in the entire history of microlensing monitoring of both Magellanic Clouds. Its light curve exhibited not only a clear parallax effect, but also a deviation to the single microlensing model around its peak. This anomaly is so tiny that it is not clearly seen in the OGLE data alone as shown in Fig. 4. However, its presence was explained with a non-caustic crossing binary lens model by Dong et al. (2007). In their analysis, they also successfully employed for the first time space-parallax effect from additional observations taken by the *Spitzer* satellite, which helped break model degeneracies and solve the microlensing event. Dong et al. (2007)

[2] http://ogle.astrouw.edu.pl/ogle3/ews/2005/smc-001.html

Table 3. Selection criteria for the search for microlensing events in the OGLE-III SMC data and the number of objects left after each cut for the All Stars and Bright Stars Samples.

Cut no.			No. of objects left	
			All	Bright
0a	Selection of 'good' objects	$N > 80$, $\langle I \rangle \leq 21.0$ mag	5470 352	
0b		$N > 80$, $\langle I \rangle \leq 19.3$ mag		1614 327
1	Significant bump over baseline	$\sum_{\text{peak}} \sigma_i > 30.0$	1217	1060
2	'Bumper' cut[a]	$\langle I \rangle > 19.0$ mag, $\langle V - I \rangle > 0.5$ mag	482	380
3	Microlensing fit better than constant line fit	$\frac{\chi^2_{\text{line}} - \chi^2_{\mu 4}}{\frac{\chi^2_{\mu 4}}{N_{\text{dof},\mu 4}} \sqrt{2N_{\text{dof},\mu 4,\text{peak}}}} > 100$	186	107
4	Number of points at the peak[b]	$N_{\text{peak}} > 5$	182	104
5	Microlensing fit better than supernova fit	$\chi^2_{\text{SN}} > \text{MIN}(\chi^2, \chi^2_{\mu 4})$	115	68
6	Peak within the data span (HJD −245 0000)	$2085 < t_0 \leq 4954$	112	65
7	Blended fit converged	$0 < f_{\text{S}} < 1.4$	35	23
8	Conditions on goodness of microlensing fit (global and at the peak)	$\frac{\chi^2}{N_{\text{dof}}} \leq 2.6$ and $\frac{\chi^2_{\mu 4,\text{peak}}}{N_{\text{dof},\mu 4,\text{peak}}} \leq 4.5$	7	6
9	Time-scale cut (d)	$1 \leq t_{\text{E}} \leq 1000$	6	5
10	Impact parameter cut	$0 < u_0 \leq 1$	3	2

[a]Magnitudes as in the field SMC100.1 (shifted according to the position of the centre of red clump).
[b]In the range of $t_0 \pm 1t_{\text{E}}$.

Table 4. Microlensing event candidates detected in the OGLE-III SMC data. Events detected by the OGLE's EWS have their EWS designation given in the name column.

Event's name (EWS)	RA (J2000.0)	Dec. (J2000.0)	Field	db Star ID	Baseline I (mag)	Baseline V (mag)	Source I (mag)	Source $V - I$ (mag)
OGLE-SMC-02 (2005-SMC-001)	0:40:28.10	−73:44:46.5	SMC128.5	15192	18.368 ± 0.002	19.389 ± 0.004	18.368 ± 0.002[a]	1.022 ± 0.005[a]
OGLE-SMC-03 (2008-SMC-001)	1:02:37.50	−73:22:25.9	SMC111.7	18094	20.66 ± 0.01	20.77 ± 0.01	20.43 ± 0.32	0.10 ± 0.01
OGLE-SMC-04	1:00:59.32	−73:14:17.1	SMC106.3	33618	18.477 ± 0.001	19.463 ± 0.005	18.69 ± 0.79	0.75 ± 0.10[b]

[a]Source brightness and colour were set to this of the event's baseline, assuming no blending and dark lens (after Dong et al. 2007).
[b]Source colour was derived using the EROS B-band data.

concluded that the most likely location of the lens is the Galactic halo, and with no light detected from the lens they suggested that the lens is a binary black hole (BH) with a total mass of around $10\,\text{M}_\odot$. Nevertheless, they have not completely excluded the SL scenario with both source and the lens residing in the SMC.

In our study, we performed a simple modelling of a single point lens event with no parallax included. This was the model we used in the automated search pipeline; therefore, we were able to derive the detection efficiency for this event. The values of the fitted parameters are gathered in Table 4, and the fit is shown in Fig. 4. The time-scale of $t_{\text{E}} = 190.6 \pm 1.6$ d we obtained for I and V data is conveniently in rough agreement with the time-scale derived by Dong et al. (2007) (between 160 and 190 d, depending on the details of the model configuration).

The blending parameters for both the bands obtained in our model are relatively close to 1; however, not including the parallax and the binarity in our model should affect this value severely. Full modelling of this event performed by Dong et al. (2007; table 1) returned a blending fraction oscillating around zero-blending solutions, even suggesting some amount of negative blending in case of a few models.

We analysed the astrometry of the residual images of this event obtained with the DIA and measured the centroid shift caused by blending during the event with respect to its position during the baseline as measured on the superb-quality template image. The accuracy of such a centroid shift can reach a few tens of milliarcseconds for bright events. In the case of OGLE-SMC-02, we did not detect any displacement of the centroid of light, which indicates that there is no additional blending light coming from a coincidental neighbouring star. The lack of blending in microlensing models by Dong et al. (2007) was also confirmed by them with high-resolution *Hubble Space Telescope* (*HST* imaging and, along with other factors, led to the conclusion the lens in this event is either dark or very faint.

Cross-match of the lens position with available high-energy data from *ROSAT*, *XMM* (Haberl & Sturm, private communication) and *INTEGRAL* (Frankowski, private communication) returned no signal which can be associated with the BH. On the other hand, we would see the X-ray signal only if there was an accreting disc around the BH, the feature very unlikely to be present in a binary BH system. Further detailed observations and studies are required in order to confirm the BH origin of this event.

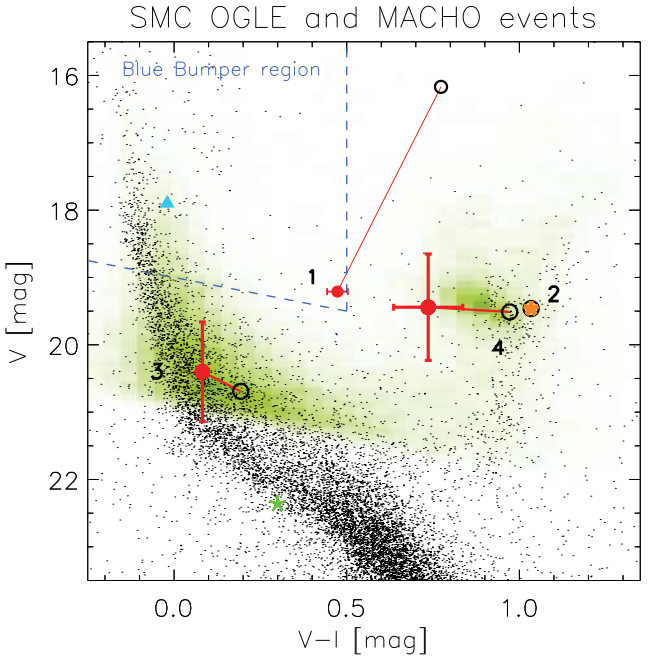

Figure 2. CMD showing *HST* (black dots) and OGLE (green) stars of one of the OGLE-III fields. Red dots show estimated colour and brightness of the source in all OGLE events, whereas black open circles indicate the baseline of each event. Blue and green dots mark MACHO events from 1997 and 1998.

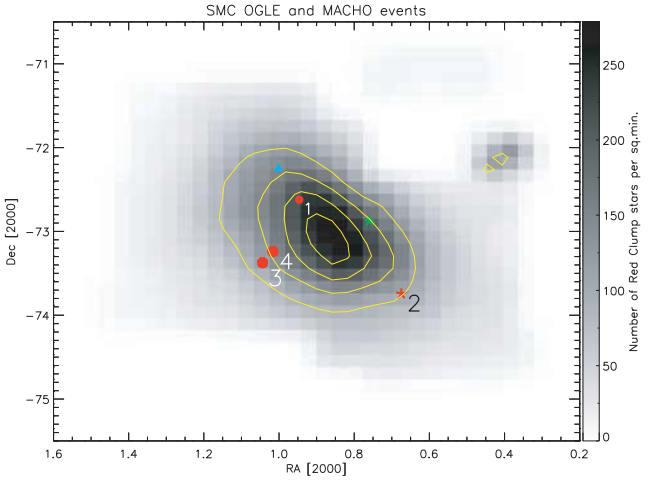

Figure 3. Localization of all SMC OGLE and MACHO events on the red clump stars' density map. The colour coding is as that used in Fig. 2. Contours follow the density of red clump stars.

4.2 OGLE-SMC-03

This event was detected in real time while it was ongoing in 2008 by the EWS (2008-SMC-001).[3] It occurred on a faint blue star but was quite well covered in both the OGLE bands (see Fig. 4), especially on the rising part of the light curve, which assures that this was not a nova-like outburst.

In order to improve the quality of the light curve of this faint object, the original data were re-reduced, so the flux variations were measured at the actual position of the event. The data were then fitted with a standard microlensing model and a model with parallax effect was included as shown in Fig. 4. The parameters of the models are gathered in Tables 5 and 6 for standard and parallax models, respectively.

All models had a strong indication of negative blending most likely caused by an underestimation of the template flux of the faint source and fringing present at the template image. This is not surprising for the object fainter than the 20th magnitude where unresolved background stars can cause local overestimation or underestimation of the background level. Removal of the lensed source following the method of Gould & An (2002) revealed no blended objects visible above the background of the images.

The position of the source of the event shown on the CMD (Fig. 2) is based on the colour and brightness of the source derived from the best microlensing fit with the negative blending, but the uncertainty caused by this effect is encoded in the large error bar of the source brightness.

Because the event was relatively long (it lasted for about 100 d), we also investigated if the parallax model can reproduce the data better than the standard model. The modelling with Markov chain Monte Carlo (MCMC) found four equally valid parallax solutions covering all possible degeneracies. Their χ^2 for multiband data fit, however, differed insignificantly ($\Delta\chi^2 \approx 0.4$; see Table 6) and were better by $\Delta\chi^2 \approx 3.4$ than the best non-parallax model with $\chi^2 = 784.13$.

We adopted the geocentric formalism to describe the parallax effects (An et al. 2002; Gould 2004), where we assume the reference system to be located at the Earth at the time $t_{0,\rm par} = 2454\,476.23$, which we choose close to the peak of the event. This ensures that the values of u_0, t_0 and $t_{\rm E}$ in the parallax model are close to those from non-parallax model. Any deviations of the observer position due to Earth motion are calculated against this reference system, which is in rectilinear motion at the velocity of the Earth at that time. The heliocentric velocity of the reference system projected on the plane perpendicular to the line of sight is approximately 29 km s^{-1} to the south. Usage of the geocentric system helps us to find and identify all degenerate solutions.

To find all solutions, we investigated the fourfold microlensing degeneracy that is created in the case of a single lens with parallax from the two coexisting discrete degeneracies: a twofold u_0 degeneracy (Smith, Mao & Paczyński 2003) and the jerk-parallax degeneracy (Gould 2004). These yield four solutions that are presented in Figs 6 and 7 – fit parameters for solutions 1 though 4 are gathered in Table 6.

Pairs of parallax solutions indicate either very close (solutions 3 and 4) or a bit more distant lens (solutions 1 and 2). The former would yield a distance to the lens of order of 100 pc for a typical mass of the lens $\sim 0.3\,{\rm M}_\odot$ – it is extremely unlikely for the potential lens to be located so close to the observer. On the other hand, the latter set of solutions have parallax scale of $\pi_{\rm E} = 0.69 \pm 0.32$. This yields a distance of 2.2 ± 4.3 kpc for a typical mass, and since it covers significantly more volume in the Galaxy and many more potential lenses, we choose these as preferred solutions. The detection of the parallax signal in this event implies that the lens most probably comes from the Galactic thick-disc population of stars.

Assuming the microlensing source to be at the distance of the SMC, as suggested by the CMD location of the source, we can neglect source motion and calculate lens velocity projected on the Earth plane to be au $\pi_{\rm E}^{-1}\, t_{\rm E}^{-1} \approx 50\,{\rm km\,s^{-1}}$. This, when taking into account the angle of the relative lens motion and the velocity of the geocentric reference system, leads to heliocentric lens velocity,

[3] http://ogle.astrouw.edu.pl/ogle3/ews/2005/smc-001.html

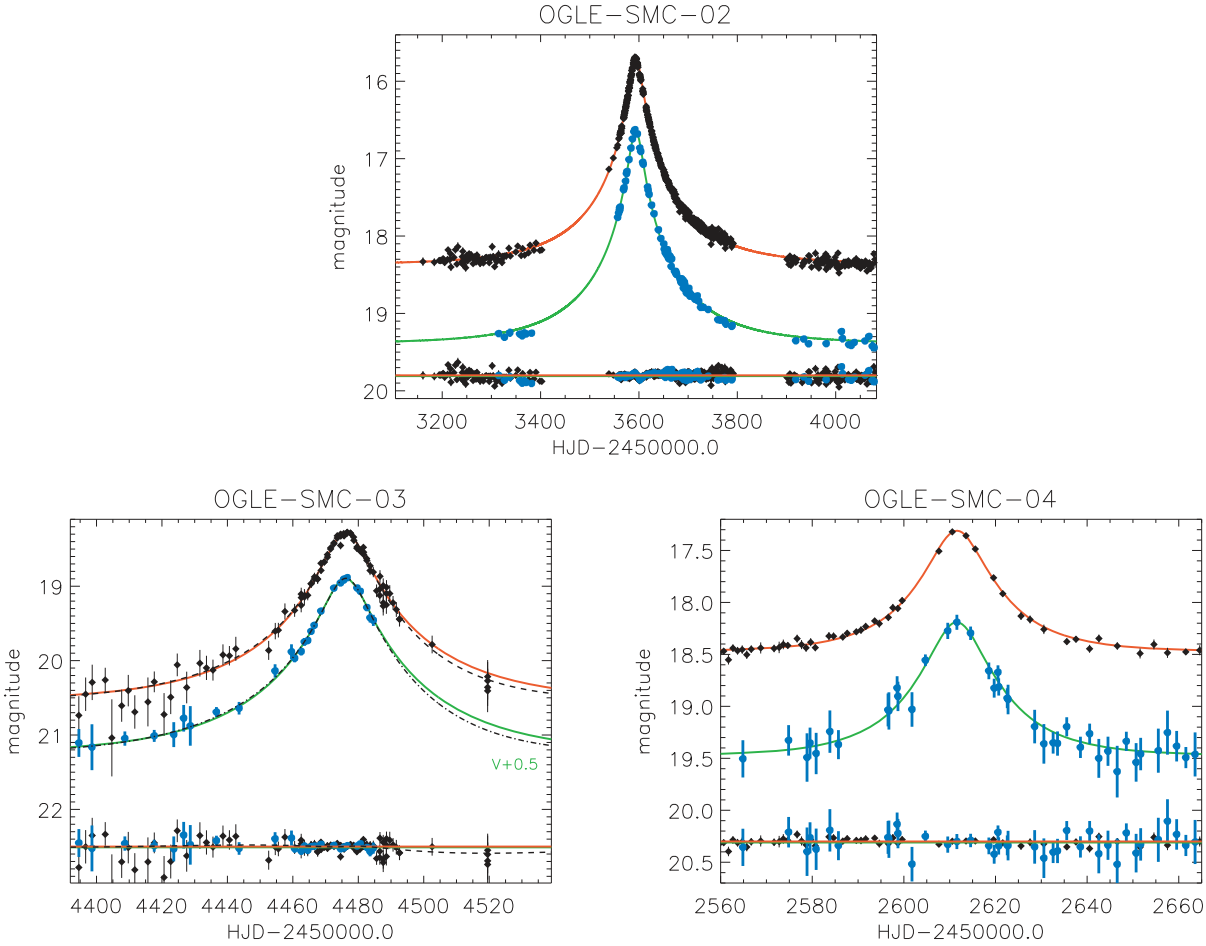

Figure 4. Light curves and microlensing models of candidates for microlensing events detected in the OGLE-III SMC data. The standard microlensing model best fitting to the data is shown in solid lines with black points and red curve for *I* band, and blue points and green curve for *V*-band data (except OGLE-SMC-04, where it shows EROS *B*-band data). Dashed line shows parallax model fit. The residuals of the model fitting are shown as respective lines and data points at the bottom of each panel.

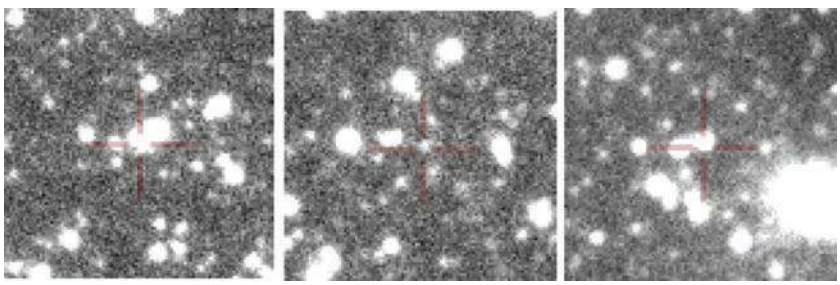

Figure 5. Finding charts of the three candidates for microlensing events from OGLE-III SMC data. East is to the right and north is down. The side of each chart is 26 arcsec. Charts with events 02, 03 and 04 are shown from left to right. A cross marks the object on which the microlensing brightening was detected.

projected on the plane of the observer, to be approximately −70 and 30 km s^{-1} in the north and the east directions, respectively. Since the lens is much closer than the source, we can neglect the effect of projection and note that the true heliocentric velocity of the lens will be of the same order. This type of kinematics is not surprising for the thick-disc object.

Because there is no blend visible, we can derive an upper limit on the lens brightness equal to around 21.5 mag in the *I* band. This limit is met by a late M dwarf (with mass $\lesssim$0.2 M$_\odot$) at a distance of more than 1.5 kpc and by an early M dwarf (with mass $\lesssim$0.3 M$_\odot$) at a distance of more than 5 kpc. Although we cannot rule out the lens to be a dark object in the Galactic halo, the lens as a disc star is a much more natural explanation. Calchi Novati & Mancini (2011) showed in their simulation of the microlensing rate towards the LMC that the contribution of the Galactic disc lenses to the overall microlensing rate is comparable to the contribution from the LMC SL. It means that in our searches for microlensing events towards Magellanic Clouds, we should expect some of them to be caused by Galactic lenses.

We can conclude that the most likely scenario for OGLE-SMC-03 is that the lens is an M dwarf with a mass of about 0.1–0.3 M$_\odot$ located 1–5 kpc from the Earth and belonging to the thick disc of the

Table 5. Parameters of the standard Paczyński microlensing model fits to the OGLE-III SMC events.

OGLE-SMC-02						
Parameter	Five-parameter fit		Four-parameter fit		Seven-parameter fit	
t_0	3593.6	±0.02	3593.7	±0.02	3593.0	±0.02
t_E	195.6	±1.9	163.2	±0.3	190.6	±1.6
u_0	0.071 32	±0.082 08	0.089 15	±0.000 16	0.073 40	±0.000 71
I_0	18.37	±0.002	18.36	±0.002	18.37	±0.002
f_{S_I}	0.8024	±0.0089	1.0	–	0.8248	±0.0078
V_0	–	–	–	–	19.39	±0.004
f_{S_V}	–	–	–	–	0.9102	±0.0095
χ^2	2836.7		3259.0		3593.0	
$\frac{\chi^2}{N_{dof}}$	2.32		2.66		2.62	
OGLE-SMC-03						
Parameter	Five-parameter fit		Four-parameter fit		Seven-parameter fit	
t_0	4476.1	±0.1	4476.1	±0.1	4476.1	±0.1
t_E	45.5	± 6.2	54.1	±0.9	47.1	±4.4
u_0	0.147	± 0.024	0.1161	±0.0013	0.140	±0.016
I_0	20.62	±0.01	20.62	±0.01	20.63	±0.01
f_{S_I}	1.32	± 0.26	1.0	–	1.25	± 0.16
V_0	–	–	–	–	20.77	±0.01
f_{S_V}	–	–	–	–	1.20	± 0.16
χ^2	708.49		710.65		784.13	
$\frac{\chi^2}{N_{dof}}$	1.01		1.01		1.02	
OGLE-SMC-04						
Parameter	Five-parameter fit		Four-parameter fit		Seven-parameter fit[a]	
t_0	2611.6	±0.1	2611.6	±0.1	2611.6	± 0.1
t_E	18.60	$^{+1.96}_{-1.85}$	17.17	±0.27	18.3	± 1.8
u_0	0.3143	$^{+0.0595}_{-0.0472}$	0.3589	±0.0039	0.3231	± 0.050
I_0	18.477	±0.001	18.477	±0.001	18.477	± 0.001
f_{S_I}	0.84	$^{+0.22}_{-0.16}$	1.0	–	0.87	$^{+0.21}_{-0.16}$
B_0	–	–	–	–	19.48	± 0.01
f_{S_B}	–	–	–	–	1.03	$^{+0.25}_{-0.18}$
χ^2	1052.3		1052.9		1154.6	
$\frac{\chi^2}{N_{dof}}$	1.43		1.43		1.15	

[a]Fit to the OGLE *I*-band and EROS *B*-band data.

Galaxy, similar to events MACHO-LMC-5 (see e.g. Drake, Cook & Keller 2004; Gould 2004) and EROS2-LMC-8 (Tisserand et al. 2007).

With a velocity of the order of 80 km s^{-1} and a location of a few kpc from the Earth, the lens should have a noticeable proper motion of a few mas yr^{-1} and therefore should be resolvable with the *HST* in a couple of years. This would give a good opportunity to confirm the nature of this event.

4.3 OGLE-SMC-04

This event was not previously detected either by EWS (it occurred in the end of 2002 in the early season of the OGLE-III when the EWS was not yet operating) or by any other surveys. Its light curve is relatively well covered by the OGLE-III *I*-band data, but there are no observations taken during the event in the *V* band.

The event was present in the EROS2 data base, however, only in their *B* band. Therefore, we performed a multiband fit using the OGLE *I*-band and EROS *B*-band data, which resulted in instrumental colour of the source of $(B-I)_S = 0.82 \pm 0.04$. This was then transformed to standard OGLE's $V-I$ following Tisserand et al. (2007) and yielded $(V-I)_S = 1.02 \pm 0.08$. The error bar includes the systematic error from the transformation. The position of the source on the CMD (Fig. 2) indicates that it belongs to the red clump giant population of the SMC.

The time-scale of the event is relatively short ($t_E = 18.3 \pm 1.8$), which favours a SL scenario. Unless the lens is nearby ($D_L < 20$ kpc), a typical time-scale of halo lensing events with masses around 0.4 M$_\odot$ and sources in the SMC are well above 20 d. In SL, the time-scales are usually a few times shorter owing to much larger projected velocity, $\tilde{v}_{SL} \approx 2000$ km s^{-1}, compared to $\tilde{v}_{halo} \approx 200$ km s^{-1} for halo lenses (Boutreux & Gould 1996). This places this event as a good candidate for a SL microlensing interpretation.

Another possibility is that the lens is a thick-disc red dwarf, given the fact that the blending object must be redder than the red clump of the SMC. High-resolution imaging could potentially reveal the actual lens as the event had already happened almost 10 years ago, giving enough time for lens and source to separate.

5 BLENDING AND DETECTION EFFICIENCY

As in the previous parts of the study of the OGLE microlensing data towards the Magellanic Clouds, we carefully tackled the issue of blending in these crowded fields. Here we applied the method developed for Paper III. In brief, we simulated OGLE-III images for a range of stellar densities using deep luminosity functions of three

Table 6. Parameters of the microlensing models with parallax fitted to the event OGLE-SMC-03.

Model no.	1	2	3	4
	$u_0 > 0$	$u_0 < 0$	$u_0 > 0$	$u_0 < 0$
	$(\pi_{\mathrm{E},\perp} > -\pi_{j,\perp}/2)$		$(\pi_{\mathrm{E},\perp} < -\pi_{j,\perp}/2)$	
t_0	4476.238	4476.242	4476.25	4476.241
	± 0.085	± 0.096	± 0.11	± 0.072
t_E	47	54	56	41
	± 21	± 27	± 28	± 11
$\pi_{\mathrm{E},N}$	−0.43	−0.56	2.31	2.55
	± 0.38	± 0.40	± 0.37	± 0.39
$\pi_{\mathrm{E},E}$	0.33	0.37	0.35	0.30
	± 0.23	± 0.25	± 0.25	± 0.22
u_0	0.148	−0.140	0.145	−0.152
	± 0.036	± 0.039	± 0.039	± 0.033
I_0	20.62	20.62	20.62	20.62
	± 0.01	± 0.01	± 0.01	± 0.01
f_{S_I}	1.41	1.35	1.49	1.47
	± 0.34	± 0.42	± 0.36	± 0.35
V_0	20.77	20.77	20.77	20.77
	± 0.01	± 0.01	± 0.01	± 0.01
f_{S_V}	1.47	1.39	1.54	1.54
	± 0.35	± 0.42	± 0.36	± 0.38
χ^2	780.80	780.80	780.49	780.39
$\frac{\chi^2}{N_\mathrm{dof}}$	1.0180	1.0180	1.0176	1.0175

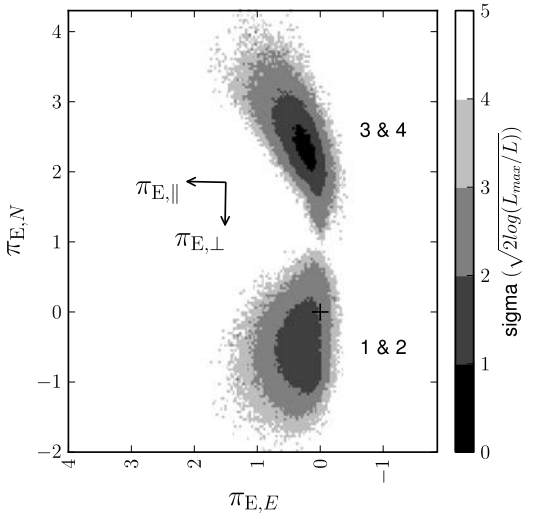

Figure 6. Likelihoods of the north and east components of the parallax signal detected in OGLE-SMC-03 event. Two regions corresponding to solutions 1 and 2 and, 3 and 4 are created through the jerk-parallax microlens degeneracy. The directions parallel (∥) and perpendicular (⊥) to the Sun's apparent acceleration in the geocentric frame are also shown (see fig. 3 in Gould 2004). Grey-scale contour shows boundaries of σ levels, which correspond to the ratios of the likelihoods of the given region (L) to the most likely region (L_max), as derived with MCMC. The black cross marks the origin of the coordinate system.

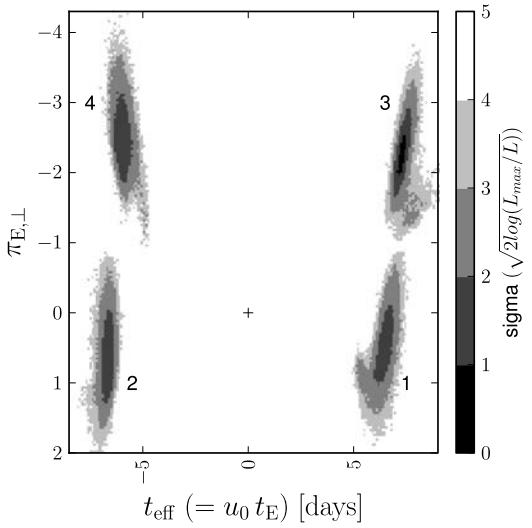

Figure 7. Four microlensing solutions generated by the jerk-parallax degeneracy and the u_0 degeneracy in the plane of t_eff and $\pi_{\mathrm{E},\perp}$. $\pi_{\mathrm{E},\perp}$ is a projection of the parallax vector on to the direction perpendicular to the Sun's acceleration in the geocentric frame at the specified time $t_{0,\mathrm{par}}$ – this is the natural coordinate for the jerk-parallax degeneracy. We use t_eff instead of u_0 since this parameter yields much smaller scatter. Numbers indicate the individual solutions from Table 6.

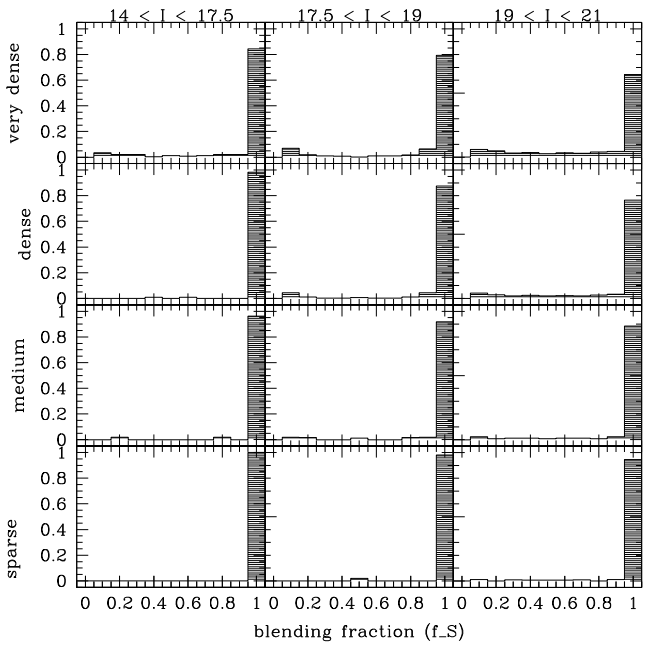

Figure 8. Distributions of blending parameter (source flux fraction in baseline flux) for selected levels of stellar density derived for the simulated OGLE-III SMC images based on deep archival *HST* images. The distributions are shown for three magnitude bins. The density levels shown correspond to stellar densities of log (N_*/CCD chip) = (4.9, 4.6, 4.4, 3.9) for very dense, dense, medium and sparse fields, respectively.

representative fields from the *HST* Local Group Stellar Photometry archive (Holtzman, Afonso & Dolphin 2006). Locations of the selected fields are marked in Fig. 1. Then we compared simulated OGLE images with the input catalogue of stars and were able to assign a number of real *HST* stars to each blended object detected on a simulated frame. For each density level and in three magnitude bins, $14 < I < 17.5$ (bright), $17.5 < I < 19$ (medium) and $19 < I <$ 21 (faint), we derived a distribution of flux ratio between each *HST* component and the blended object it was residing in. The blending distributions are shown in Fig. 8. We were also able to calculate a mean ratio between the number of real stars and all the objects composed of these stars. This ratio was then used as a CF for observed OGLE template images in order to estimate the real number

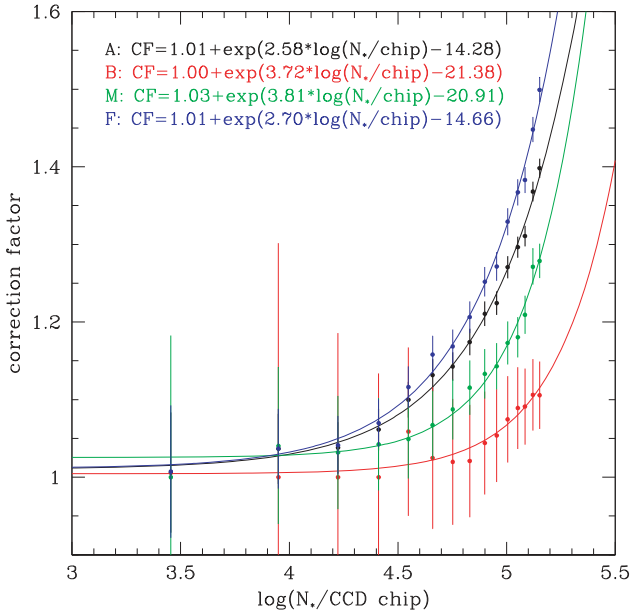

Figure 9. CF for the number of monitored stars as a function of the density of the stars on a single CCD chip of the OGLE-III template image. Shown are the CFs for three magnitude bins (B for bright, M for medium and F for faint) and for the entire magnitude range (A for all). The legend shows the expression for the curve fitted to each of the data sets.

of monitored stars in each field (see Table 1). The CF is shown in Fig. 9 for all stars (A) and three magnitude bins: bright (B), medium (M) and faint (F).

With these blending distributions at hand, we were able to perform the detection efficiency determination. For selected fields representing different density levels and for time-scales in the range between 1 and 1000 d, we simulated numerous microlensing events with the parameters being drawn from realistic distributions. For the lensed flux, we used the measurements of randomly selected star from the simulated field, which during the event was split between blend and source according to the blending parameter. This procedure also preserved any variability of the underlying flux, allowing for events with variable baseline (see e.g. Wyrzykowski et al. 2006).

The efficiency curves for representative dense and sparse fields and for the All Stars and Bright Stars Samples are shown in Fig. 10. The detection efficiencies do not change much with the density of the field due to relatively low gradient in the stellar density in the OGLE-III SMC fields. The calculated efficiency is somewhat lower when compared with the one obtained for OGLE-III LMC data, mainly because here we used a different magnitude cut on star selection for the All Stars Sample (21.0 mag, compared with 20.4 mag for the LMC).

6 OPTICAL DEPTH

Having the three events and their time-scales as well as the detection efficiency of each of them, we are able to calculate the average optical depth towards the SMC based on OGLE-III data. In order to evaluate equation (2), we also need the estimated number of total monitored stars, derived in the previous section, and the total time of observation, $T_{\rm obs} = 2870$ d.

First, we calculated the optical depth for the All Stars Sample ($N_* = 5971\,776$, down to $I = 21$ mag) using the detection efficiencies obtained in our simulations. Because our simulations utilized I-band data solely, we used $t_{\rm E}$ obtained in a five-parameter fit for all

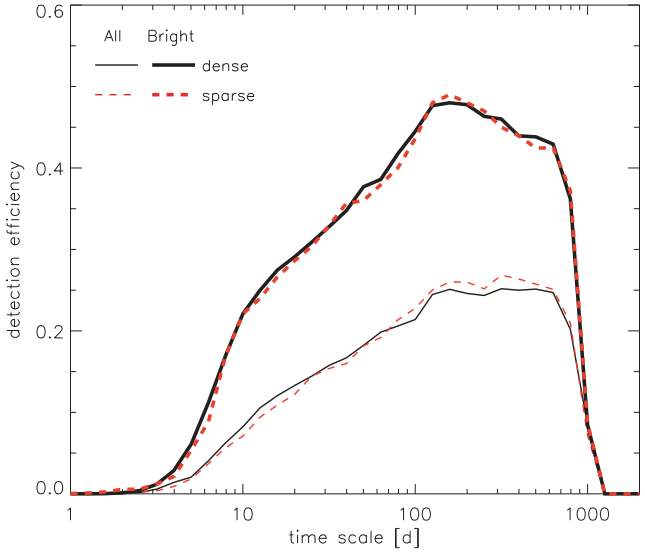

Figure 10. Microlensing event detection efficiency, for example dense (solid lines, field SMC106.3) and sparse (dashed lines, field SMC111.7) fields of the SMC as observed by OGLE-III. Shown are curves for All Stars Sample and Bright Stars Sample (thin and thick lines, respectively).

the three events. This led to total $\tau_{\rm SMC-OIII} = 1.17 \pm 0.91 \times 10^{-7}$. The error on τ was calculated following Han & Gould (1995) and reflects only the uncertainty caused by the small number of events used.

Then, similarly as in Papers I, II and III, we corrected the efficiency for the fact that our simulations were only considering single-point events and that lensing by a binary (and other exotic effects) was not included. Efficiencies were scaled down by 10 per cent, and the optical depth for efficiency corrected for binary events was $\tau_{\rm SMC-OIII} = 1.30 \pm 1.01 \times 10^{-7}$. Details of the calculations for each event are shown in Table 7.

For the Bright Stars Sample ($N_* = 1702\,724$, down to $I = 19.3$ mag), the optical depth calculated for two events (#2 and #4) is $\tau_{\rm SMC-OIII} = 1.52 \pm 1.40 \times 10^{-7}$ and $1.69 \pm 1.55 \times 10^{-7}$, when efficiencies were corrected for lack of sensitivity for binary events. Within the (large) error bars, the estimates of the optical depth for the All Stars and Bright Stars Samples are in agreement. However, it

Table 7. The optical depth for the three events found in the OGLE-III SMC data calculated for the All Stars Sample. The columns show event name, its time-scale, detection efficiency and individual event's contribution to the total optical depth.

Event	$t_{\rm E}$	$\epsilon(t_{\rm E})$	$\tau_i \times 10^{-7}$
Efficiency not corrected for binary events			
OGLE-SMC-02[a]	195.6 ± 1.9	0.234 942	0.76
OGLE-SMC-03[a]	45.5 ± 6.2	0.155 922	0.27
OGLE-SMC-04	$18.60^{+1.96}_{-1.85}$	0.123 365	0.14
total $\tau_{\rm SMC-OIII}$			1.17 ± 0.91
Efficiency corrected for binary events			
OGLE-SMC-02[a]	195.6 ± 1.9	0.211 448	0.85
OGLE-SMC-03[a]	45.5 ± 6.2	0.140 330	0.30
OGLE-SMC-04	$18.60^{+1.96}_{-1.85}$	0.111 028	0.15
total $\tau_{\rm SMC-OIII}$			1.30 ± 1.01

[a]Time-scale and efficiency for these events are taken from a standard fit.

is clearly seen that higher detection efficiency does not completely counterbalance the smaller number of stars and smaller number of events in the Bright Stars Sample.

Note that the binary-lens event OGLE-SMC-02 was included in the optical depth calculations above as if it were a standard event. This approximation is justified because even though the light curve of this event deviates a little from the standard 'Paczyński' curve, the event passes through our automated pipeline, which does not consider any exotic effects. Moreover, the time-scale obtained in the standard fit is very close to the one obtained in the full model by Dong et al. (2007). Therefore, it was also possible to derive the detection efficiency for this event. The same applies to the parallax event OGLE-SMC-03.

7 DISCUSSION

In the 8 years of the OGLE-III data covering the SMC and its surroundings, we detected three convincing microlensing event candidates.

This is definitively the best set of candidates presented in the series of our papers concerning microlensing searches towards the Magellanic Clouds with the OGLE data. The microlensing nature of all three events is very difficult to disprove – none of their sources is located in the region of potential contaminant 'blue bumpers' (Fig. 2), and their light curves covering at least 8 years (12 years for OGLE-SMC-02 as it was also monitored during the OGLE-II) show no other additional bumps. Additional data spanning for a couple of more years available for all three events from the MACHO and EROS groups also show no further bumps.

However, still the most difficult question to answer is where these events originated from. In principle, because standard microlensing model cannot tell us where the source and the lens are located, there are a number of different combinations possible, including the SMC, the halo of the Milky Way (MW) and the disc of the MW. In the history of the Magellanic Cloud microlensing, there were already examples of confirmed cases of each of the combinations, e.g. source and lens from the SMC (Assef et al. 2006), disc lens towards the LMC (Kallivayalil et al. 2004).

In the case of our events, the new one, OGLE-SMC-04, is probably the best candidate for SL event given its time-scale and location in the red clump stars of the SMC; however, we cannot exclude the thick-disc red dwarf scenario or MACHO. The parallax effect detected in the event OGLE-SMC-03 helps constrain the lens to most likely be a typical M dwarf star from the Galactic disc; however, a dark lens cannot be entirely ruled out. Finally, even though OGLE-SMC-02 is likely to be a halo lens, Dong et al. (2007), who modelled it in detail, did not exclude the SL option completely.

The effect of SL for the SMC is not yet well understood. However, due to the alignment of the SMC along the line of sight, the contribution of SL to τ is expected to be higher than in the face-on LMC and be at least 1.0×10^{-7}, in average (Palanque-Delabrouille et al. 1998; Graff & Gardiner 1999). This is in good agreement with the value of the optical depth we measured for all three events found in the OGLE-III data. Therefore, we expect the signal from SL or, more generally, the background of lensing by known stellar populations, to be close to what we have detected. However, because the nature of our events is not yet firmly confirmed, we can derive an upper limit on dark matter compact halo objects, following Alcock et al. (2001), Tisserand et al. (2007) and Papers I, II and III.

Assuming the MACHO mass distribution function from model 'S' from Alcock et al. (2000) and using the mean detection efficiency for our SMC fields, we derived the number of expected events due to MACHOs as a function of their mass. The mass in such events can be approximately translated to a time-scale as $\log M = 2\log(t_{\rm E}/70)$. The number of expected events compared with the observed (or not observed) signal can be converted to an upper limit on the MACHO halo mass fraction using enhanced Poisson statistics with background signal (Feldman & Cousins 1998). The derived upper limit for OGLE-III SMC data is shown in Fig. 11 and was calculated assuming we expect about three events from the SL/background. For a 'typical' MACHO with mass of $0.4\,{\rm M}_{\odot}$, the fraction is less than 37 per cent, but for lower masses, between 0.01 and $0.1\,{\rm M}_{\odot}$ it is below 20 per cent. Fig. 11 shows also an upper limit on MACHOs derived by EROS (Tisserand et al. 2007) and MACHO signal claimed by the MACHO group at 95 per cent confidence. For the latter, we show both the original value from Bennett (2005) (for $\tau = 1.0 \pm 0.3 \times 10^{-7}$) for all MACHO events being due to MACHOs and the value corrected following the rejection of one of the original MACHO events (MACHO-LMC-7; see Paper III). For the corrected value, the MACHO fraction in the halo becomes 18 per cent, compared to the original 20 per cent. If the background lensing (Galactic disc and LMC SL) was extracted from the MACHO signal (at a conservative level suggested in Bennett 2005 of 0.24×10^{-7}) and the compromised event was rejected, the MACHO group data can be interpreted that only about 14 per cent of MACHOs may compose the Galactic halo.

We can obtain a much tighter limit from OGLE by combining all OGLE-II and OGLE-III results for both LMC and SMC. For each set of data, we computed the expected number of events for a given mass of the deflector and combined it with about eight events expected to be due to the background lensing populations. It yielded $f < 0.06$ (at 95 per cent confidence level) for masses around $0.4\,{\rm M}_{\odot}$ and reached the minimum of $f < 0.04$ at mass range between 0.01 and $0.15\,{\rm M}_{\odot}$. Fig. 12 shows the combined OGLE limit along with the corrected MACHO group signal and EROS upper limit with both the axes zoomed in at the intersection of results from all surveys. This result, therefore, pushes the upper limit on MACHO mass fraction in the halo down to a value similar to the one derived by EROS. The OGLE result is somewhat more sensitive to MACHOs in the higher mass regime (between 1 and $10\,{\rm M}_{\odot}$), and is significantly less sensitive for masses below $0.01\,{\rm M}_{\odot}$.

When looking at all events in more detail, in the most likely case, we can safely attribute to non-MACHO lensing (SL or disc lensing) all the events detected in the LMC and SMC during OGLE-II and OGLE-III, except OGLE-SMC-02. In such case, the optical depth due to this single dark matter event would be $\tau_{\rm SMC\#2} \approx 0.12 \times 10^{-7}$. If the MW halo were composed only from such lenses with mass of around $10\,{\rm M}_{\odot}$, then such an optical depth would mean that they contribute no more than 2 per cent of the total mass of the dark halo. This is in agreement with the expected mass fraction of BHs in the total mass budget of the Galaxy varying from around 5 per cent (Sartore & Treves 2010) for all massive stellar remnants to 0.4 per cent for a standard initial mass function (e.g. Bastian, Covey & Meyer 2010) integrated above $6\,{\rm M}_{\odot}$. It is also a much tighter limit than the limit of 40 per cent derived by the MACHO group on objects below $30\,{\rm M}_{\odot}$ (Alcock et al. 2001), obtained based on a lack of long-term events. The value obtained for a single microlensing event, however, is only crudely estimated, and should be assessed more elaborately, e.g. with simulations of long events in the OGLE-II and OGLE-III data combined. In practice, more events with long time-scales are needed in order to put better and more statistically sound constraints on the massive stellar remnant abundance in the halo. Continued observations of the Magellanic Clouds by MOA and

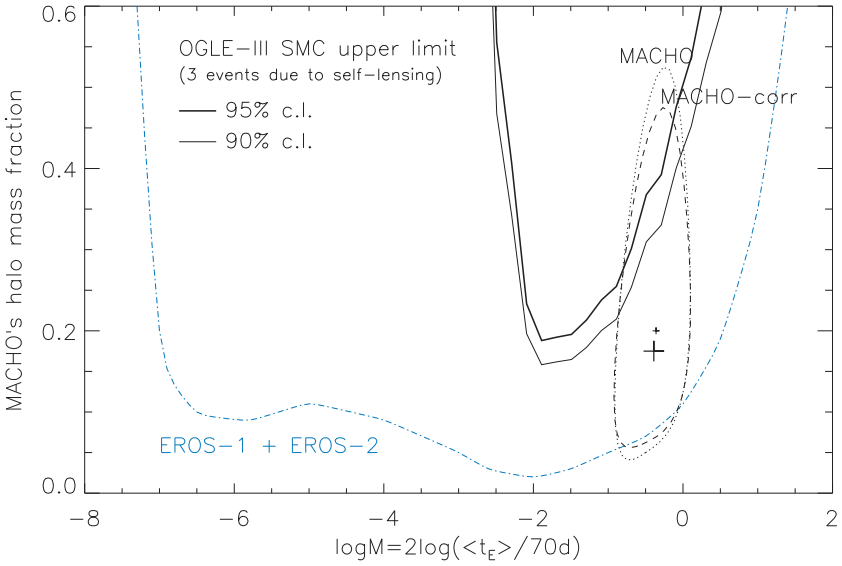

Figure 11. Fraction of the mass of MACHOs in the halo as derived from the OGLE-III SMC data. Black solid curves show an upper limit from the OGLE-III SMC data assuming the background SL signal of the three events. Also shown is the upper limit from EROS (blue dashed curve), original measurement by MACHO (small cross and dotted curve) and the MACHO result corrected for the fact that one of their events was rejected by the OGLE-III data (dashed curve, big cross).

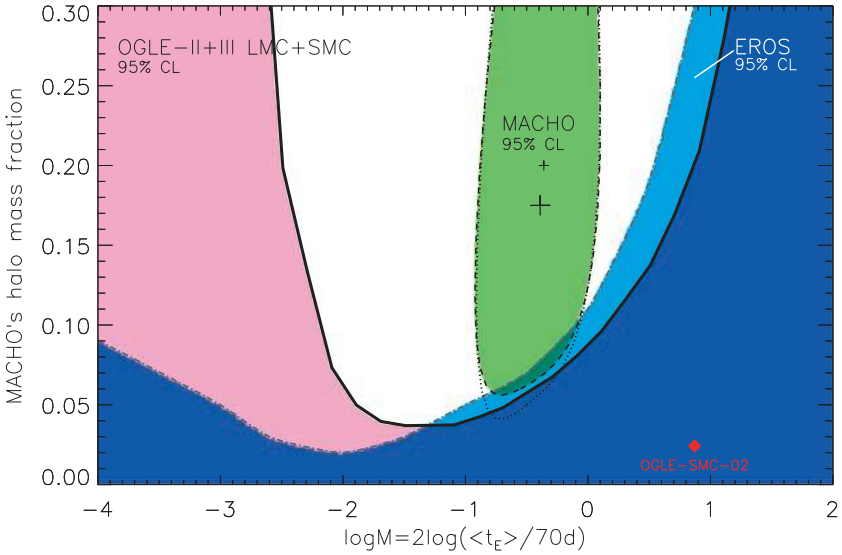

Figure 12. Inclusion region for the fraction of the mass of MACHOs in the halo for the combined OGLE-II and OGLE-III data for LMC and SMC (solid curve, pink/dark blue) when all OGLE events are attributed to expected SL/background signal. The EROS upper limit and the MACHO signal are shown as in Fig. 11 in light/dark blue and green, respectively. Also shown is the fraction of mass due to BH-candidate event OGLE-SMC-02

OGLE-IV surveys will hopefully yield more potential BH events residing in the halo if they are common enough.

8 CONCLUSIONS

We analysed OGLE-III data covering the SMC and found three convincing candidates for microlensing events, among which one was not known before (OGLE-SMC-04). Two of the events are likely to be caused by SL or have lenses located in the Galactic disc. OGLE-SMC-03 is actually the first event towards the SMC exhibiting clear parallax signal, which makes the lens likely to be in the thick disc. The third one (OGLE-SMC-02) is a potential candidate for a binary BH lens from the halo, but its SL origin cannot be totally excluded.

Following a detailed analysis of the blending in the SMC, we derived the optical depth for the All Stars Sample of $\tau_{\rm SMC-OIII} = 1.30 \pm 1.01 \times 10^{-7}$, which is in agreement with the expected SL signal towards the SMC. The upper limit on the dark matter in the form of MACHOs derived for the OGLE–III SMC data alone was about 20 per cent for masses below $0.1\,{\rm M}_{\odot}$.

In this paper, we concluded the studies of the microlensing searches conducted so far by the OGLE project towards the Magellanic Clouds. We presented the final result combining all available data and deriving new constraints on the fraction of massive compact halo objects in the Galactic halo of 6 per cent for $M = 0.1$–$0.4\,{\rm M}_{\odot}$

and below 4 per cent for lower masses. For MACHOs with mass of 1 and 20 $M_{\odot}$, the upper limits are $f < 9$ and $f < 20$ per cent, respectively. 13 years of OGLE observations indicate that the MACHO halo fraction is well below the value suggested by MACHO group (14 per cent after correction due to rejection of one of their events owing to a second bump for the same events found in the OGLE data) and in agreement with the limit derived by EROS survey.

Our result indicates that baryonic dark matter in the form of relics of stars and very faint objects in the subsolar mass regime is unlikely to inhabit the MW's dark matter halo in any significant numbers. The presence of the BH lens candidate towards the SMC agrees with the expected <2 per cent contribution of BHs to the mass of the Galactic halo.

With the OGLE project now in its fourth phase, we hope the sensitivity to extremely long events will improve significantly within the next years when combined with the historic OGLE data. Long-duration events will also be easily detectable in near real time by *Gaia* satellite, due to launch in 2013. Detailed follow-up observations of the alerts triggered by OGLE and *Gaia* will be crucial for revealing the true nature of detected events. This should result in an increase in the number of potential BH lenses or allow us to rule out heavy dark matter compact objects as well and close that topic definitively.

ACKNOWLEDGMENTS

We would like to thank the referee, Andy Gould, for comments which improved the paper significantly. We also would like to thank for their help at various stages of this work Drs Nicholas Rattenbury, Vasily Belokurov, Martin Smith and Subo Dong. We also thank Drs Adam Frankowski, Frank Haberl and Richard Sturm for their help with high-energy data. This work was partially supported by EC FR7 grant PERG04-GA-2008-234784 to ŁW. JS acknowledges support through the Polish MNiSW grant no. N20300832/070 and Space Exploration Research Fund of The Ohio State University. The OGLE project acknowledges funding received from the European Research Council under the European Community's Seventh Framework Programme (FP7/2007-2013), ERC grant agreement no. 246678.

REFERENCES

Alard C., Lupton R. H., 1998, ApJ, 503, 325
Alcock C. et al., 2000, ApJ, 542, 28111
Alcock C. et al., 2001, ApJ, 550, L169
An J. H. et al., 2002, ApJ, 572, 521
Assef R. J. et al., 2006, ApJ, 649, 954
Bastian N., Covey K. R., Meyer M. R., 2010, ARA&A, 48, 339
Bennett D. P., 2005, ApJ, 633, 906
Boutreux T., Gould A., 1996, ApJ, 462, 705
Calchi Novati S., 2010a, preprint (arXiv:1001.2388)
Calchi Novati S., 2010b, Gen. Relativ. Gravitation, 42, 2101
Calchi Novati S., Mancini L., 2011, preprint (arXiv:1105.4615)
Calchi Novati S., Mancini L., Scarpetta G., Wyrzykowski Ł., 2009, MNRAS, 400, 1625
Dilday B. et al., 2010, ApJ, 713, 1026
Dong S. et al., 2007, ApJ, 664, 862
Drake A. J., Cook K. H., Keller S. C., 2004, ApJ, 607, L29
Feldman G. J., Cousins R. D., 1998, Phys. Rev. D, 57, 3873
Gould A., 2004, ApJ, 606, 319
Gould A., An J. H., 2002, ApJ, 565, 1381
Graff D. S., Gardiner L. T., 1999, MNRAS, 307, 577
Han C., Gould A., 1995, ApJ, 449, 521
Holtzman J. A., Afonso C., Dolphin A., 2006, ApJS, 166, 534
Kallivayalil N., Nguyen H. T., Werner M. W., Alcock C., Patten B. M., Stern D., 2004, BAAS, 36, 725
Mancini L., Calchi Novati S., Jetzer P., Scarpetta G., 2004, A&A, 427, 61
Moniez M., 2010, Gen. Relativ. Gravitation, p. 13
Paczyński B., 1986, ApJ, 304, 1
Paczyński B., 1996, ARA&A, 34, 419
Palanque-Delabrouille N. et al., 1998, A&A, 332, 1
Sahu K. C., 1994a, PASP, 106, 942
Sahu K. C., 1994b, Nat, 370, 275
Sartore N., Treves A., 2010, A&A, 523, A33
Smith M. C., Mao S., Paczyński B., 2003, MNRAS, 339, 925
Smith M. C., Woźniak P., Mao S., Sumi T., 2007, MNRAS, 380, 805
Sumi T. et al., 2006, ApJ, 636, 240
Tisserand P., Le Guillou L., Afonso C., Albert J. N., The EROS-2 Collaboration et al., 2007, A&A, 469, 387
Udalski A., 2003, Acta Astron., 53, 291
Udalski A., Szymanski M. K., Soszynski I., Poleski R., 2008, Acta Astron., 58, 69
Woźniak P. R., 2000, Acta Astron., 50, 421
Wyrzykowski Ł., Udalski A., Mao S., Kubiak M., Szymański M. K., Pietrzyński G., Soszyński I., Szewczyk O., 2006, Acta Astron., 56, 145
Wyrzykowski Ł. et al., 2009, MNRAS, 397, 1228 (Paper I)
Wyrzykowski Ł. et al., 2010, MNRAS, 407, 189 (Paper II)
Wyrzykowski Ł. et al., 2011, MNRAS, 413, 493 (Paper III)

This paper has been typeset from a TEX/LATEX file prepared by the author.